Simultaneously realizing thermal and electromagnetic cloaking by multi-physical null medium

Yichao Liu, Xiaomin Ma, Kun Chao, Fei Sun*, Zihao Chen, Jinyuan Shan, Hanchuan Chen, Gang Zhao and Shaojie Chen

Key Lab of Advanced Transducers and Intelligent Control System, Ministry of Education and Shanxi Province, College of Physics and Optoelectronics, Taiyuan University of Technology, Taiyuan 030024 China.

*Correspondence: F Sun, E-mail: sunfei@tyut.edu.cn

This file includes:

Supplementary information for this paper is available at https://doi.org/10.29026/oes.2024.230027

Section 1: Numerical method and settings

The numerical simulations are all conducted by commercial software COMSOL Multiphysics 5.6 with the license number 9406999 (https://www.comsol.com), which is based on the finite element method.

The solid heat transfer module with steady-state solver is chosen to simulate the temperature field distributions and verify the thermal performance of the designed devices. In Figs. 2(e, g, i), 3(h, n, p) and 4(f, j), a fixed low temperature T_l=0 °C is set for the outer boundaries, a line source with fixed heat power of Q = 10 W/m is set as the heat source in Figs. 2(e, i), 3(h, n, p) and 4(f, j), and a surface heat source with fixed high temperature T_h=100 °C is set for the root of the fractal tree in Fig. 2(g). In Figs. 3(f, j, l), 4(d, h) and 5(c, e), fixed temperatures T_h=100 °C and T_l=0 °C are chosen as the left and right boundaries, respectively, and other side boundaries are set to be thermal insulation. In Figs. 3(f, h) and 4(h, j), thermal insulation boundaries are set around the concealed region. Normalized thermal conductivity, thermal capacity, and mass density are used for the ideal TENM in Figs. 2 and 3, i.e., κ_b = 1 W/m/K, c_b = 1 J/kg/K, ρ_b =1 kg/m³. The thermal conductivity of the ideal TENM in Fig. 2 and 3 is set to be 10000 W/m/K along the principal axes and 0.0001 W/m/K along the direction perpendicular to the principal axes. The thermal conductivity of the concealed region in Fig. 3 is set to be 0.001 W/m/K. In Figs. 4 and 5, the thermal conductivities of various materials in simulations are chosen as copper κ_c=400 W/(m·K), expanded polystyrene κ_p=0.04 W/(m·K), and static air κ_a=0.024 W/(m·K), which are derived from experimental measurements[S1–S4]. The free tetrahedral and triangular meshing are chosen for 3D simulations in Fig. 5 and 2D simulations in other figures, respectively.

In Figs. S1(d, e), and S3(d), a fixed low temperature T_l=0 °C is set for the outer boundaries, and a surface heat source with fixed high temperature T_h= 100 °C is set for the left input ports. In Fig. S4(d), a fixed temperature T_h=25 °C is set for the outer boundaries, and a fixed temperature of T_l=0 °C is set as the temperature of a thermal cooler. In Fig. S5(d), a fixed low temperature T_l=0 °C is set for the outer boundaries, and a line source with fixed power Q= 10 W/m is set as the heat source. In Figs. S2(d), S5(b, f, h), the input and output boundaries are set as fixed temperatures T_h= 100 °C and T_l=0 °C, the remaining boundaries of the thermal bender and the boundaries of the simulation area are chosen as thermal insulation boundaries. The thermal conductivity of the concealed region in Fig. S4 is set to be 0.001W/m/K.

The wave optic module with frequency domain solver is chosen to simulate the EM wave propagation and verify the electromagnetic performance of the designed devices. In Figs. 2(d, h), 3(g), 4(e, i), 5(f, g), S3(c), and S5(c), line currents are set as the sources, Gaussian beams are used for Figs. 2(f), S1(c) and S4(c), and transverse electromagnetic modes are used for other figures. Scattering boundaries are used for all the EM wave simulations except for the wave guiding part in Figs. 3(e, i, k), 4(c, g), S2(c), and S5(e), where perfect electric conductors are used as the side boundaries. In Fig. 5(f) and 5(g), all boundaries of the concealed region are set as PEC. In all simulations, we use $\boldsymbol{\varepsilon} = \boldsymbol{\mu} = diag[10000, 0.0001, 0.0001]$ for the ideal TENM, perfect electric conductors for copper, and $\varepsilon = \mu = 1$ for EPS and air. The maximum grid is set to 1/5 of the effective wavelength for each case, and the minimum grid is set to 1/50 of the effective wavelength for each case.

Section 2: Other thermal-electromagnetic devices by thermal-electromagnetic surface transformation

General design steps for thermal-electromagnetic surface transformation, i.e., the standardized black-box designing steps (see Movie S1), can be summarized as follows:

Step 1: Determine the shape of the input and output wavefront/isotherm (e.g., black and red dotted lines in Fig. 3(a)) according to the pre-designed function of the device.

Step 2: Determine the shape of the input and output boundaries of the TENM (e.g., black and red solid lines in Fig. 3(a)), which can be designed as the same with the input/output wavefront/isotherm.

Step 3: Find a proper one-to-one projection relationship that can geometrically project the points from the input boundary to output boundary of the TENM one by one (e.g., the projection indicated by the blue arrowed lines in Fig. 3(a)), which should also fulfill the function of the device and be easy for manufacture.

Step 4: Fill the region where the projection tracks exist (e.g., the region with the blue arrowed lines in Fig. 3(a)) by the TENM, whose principal axes coincide with the projection directions (i.e., the directions of the arrowed lines).

Next, we will use the above design method to design some other thermal-electromagnetic devices with various functions and applications.

Thermal-electromagnetic splitter

In many interferometric measurement systems, an EM beam splitter are needed to simultaneously generate coherent signal and reference EM waves. While for an intelligent temperature control system, it is necessary to simultaneously monitor and adjust the temperature of the target module in real-time to make it work near its rated temperature, where a thermal splitter can be utilized to simultaneously sense and cool the temperature of the target module. In some applications, especially in space-constrained on-chip systems with high integration level, both EM beam splitter and thermal splitter are required. For example, an EM beam splitter is required to split the EM wave created from an on-chip integrated EM radiator (for generating coherent signal/reference beams), and a thermal splitter is also required to produce intelligent temperature control on the EM radiator. However, the space for an on-chip system with high integration level is limited and not suitable for integrating both a thermal splitter and an EM beam splitter on it.

A thermal-electromagnetic splitter, which can simultaneously split EM waves and temperature fields into two identical parts by one structure in Fig. S1(a), can help to solve the above problem. The thermal-electromagnetic splitter can
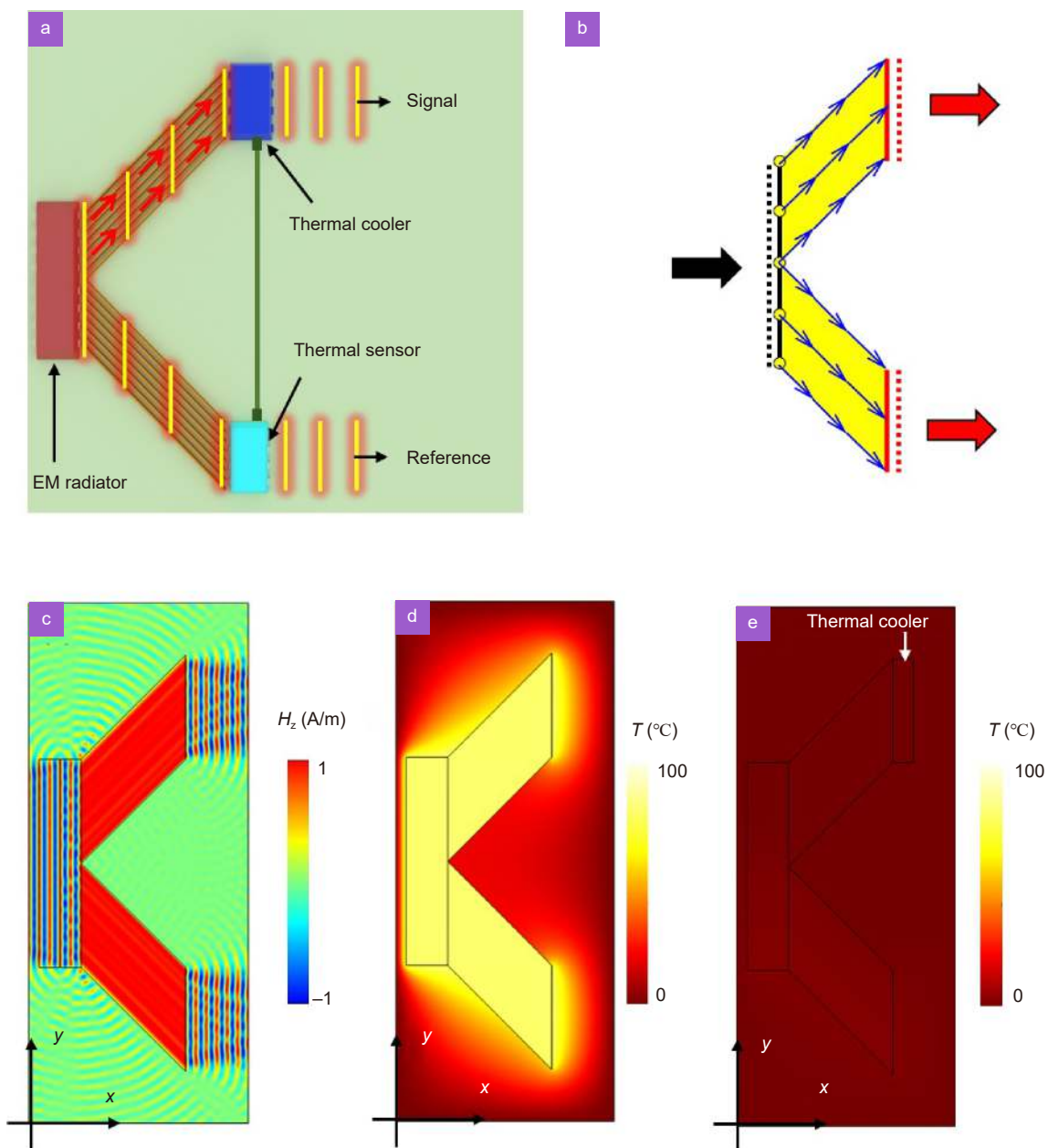

Fig. S1 | (a) An application of the thermal-electromagnetic splitter for simultaneously processing thermal-electromagnetic parallel signals on a

divide the EM wave (yellow lines in Fig. S1(a) represent the wave front) generated from the on-chip integrated EM radiator into two coherent waves (for further modulation into the signal wave and reference wave by the subsequent integration module), and simultaneously create two thermal paths connected to the EM radiator for a real-time intelligent temperature control, e.g., a thermal sensor monitoring the temperature of the EM radiator at one port of the thermal-electromagnetic splitter can feedback the real-time temperature of the EM radiator to a thermal cooler at the other port of the thermal-electromagnetic splitter, which can decide whether to cool the EM radiator based on the temperature difference between the feedback value and the rated temperature (i.e., achieving simultaneous operation of sensing module and cooling module without congestion). If the sensing module and cooling module are placed at the same port, non-invasive temperature control of the other port can be achieved. Therefore, a thermal-electromagnetic splitter can simultaneously split EM wave and heat flux without any mutual interference and congestion, which can be used to simultaneously process thermal-electromagnetic parallel signals on a highly integrated chip.

The thermal-electromagnetic splitter of above expected function, which can split an EM beam or heat flow into two parts without altering their directions, can be designed by the thermal-electromagnetic surface transformation through standardized black-box designing steps (see Fig. S1(b)):

Step 1: determine the input/output wavefront/isotherm, which is represented by three parallel dotted lines in Fig. S1(b), i.e., the longer black dotted line represents the input wavefront/isotherm and two shorter red dotted lines represent the output wavefronts/isotherms.

Step 2: determine the shape of the input and output boundaries of the TENM, which are indicated by the black solid line and red solid lines in Fig. S1(b), respectively, by choosing the same shapes as the black dotted line and red dotted lines, respectively.

Step 3: design a one-to-one projection/mapping geometrically from the points on the input boundary (the long black solid line) to the points on the output boundary (two short red solid lines), where blue arrowed straight lines in Fig. S1(b) are chosen to connect the input and output boundaries.

Step 4: fill the region where the projection tracks exist by TENM, i.e., the yellow region is filled by the TENM with its principal axes along the blue arrowed lines. Then, the TENM in the yellow region can perform as a thermal-electromagnetic splitter, which can simultaneously split EM wave and heat flux.

Figure S1(c) and S1(d) show the simulated results of the above designed thermal-electromagnetic splitter, where the splitter can split an EM wave into upper and lower branches without changing its direction of propagation in Fig. S1(c), and it can also guide heat flow propagate along the upper and lower paths in Fig. S1(d). If a thermal cooler is placed at the upper end of the splitter, the whole system can be cooled down, which is shown in Fig. S1(e).

Thermal-electromagnetic bender

The EM/Thermal bender can simultaneously perform as a radome for steering radiated/received EM signals and a thermal tube for directionally guiding the heat, which can be used in various applications. For example, an on-chip EM/Thermal bender can help to achieve radiation pattern modulation and heat flow management simultaneously of an on-chip system (e.g., electronic/photonic chips and radio-frequency/microwave circuits). For on-chip systems with high integration level, an EM/Thermal bender can be used to steer EM radiation signals produced by the on-chip radiation module (i.e., radio frequency identification devices or patch antenna), and guide the heat flux generated by the on-chip radiation module around thermal sensitive element to the cooler. In this case, the on-chip EM beam steering, thermal sensitive element protection, and specific on-chip element cooling can be achieved simultaneously with the help of one EM/Thermal bender.

Figure 2S(a) shows a 90-degree thermal-electromagnetic bender, which can simultaneously bend EM waves and heat flux by 90 degree. The EM wavefronts (indicated by the yellow line segments) produced by an on-chip antenna (red block) can be steered by 90 degree, and the waste heat generated from the on-chip antenna can also be guided by 90 degree to the thermal cooling module without touching the thermal sensitive element. The 90-degree thermal-electromagnetic bender of above expected function can also be designed by the thermal-electromagnetic surface transformation through standardized black-box designing steps (see Fig. S2(b)):

Step 1: determine the input/output wavefront/isotherm, which are drawn as the black and red dotted lines, respect-

ively. The input and output wavefront/isotherm have the same shape (i.e., plane), but there is a relative 90 degree rotation of the orientation.

Step 2: determine the shape of the input and output boundaries of the TENM, which are indicated by the black solid line and red solid lines in Fig. S2(b), respectively. The input and output boundary of the bender can be easily determined by choosing the same shapes as the input/output wavefront/isotherm, i.e., the black/red solid lines are parallel to the black/red dotted lines.

Step 3: design a one-to-one projection/mapping geometrically from the points on the input boundary (the black solid line) to the points on the output boundary (the red solid line). The blue arrowed concentric arcs in Fig. S2(b), whose center is the intersection of the black line's extension and the red line's extension, are chosen to link the input and output boundaries.

Step 4: the EM/Thermal 90-degree bender can be realized by filling TENM, whose principal axes have the same directions as the blue arrows, into the yellow region between the input and output boundaries in Fig. S2(b).

The performance of the designed 90-degree thermal-electromagnetic bender, which can guide both EM waves and heat flux smoothly from the input surface to the output surface by 90 degree, are verified by numerical simulations in Fig. S2(c) and S2(d).

Thermal-electromagnetic cylinder-to-plane converter

The on-chip antennas, whose dimensions are on the order of EM wavelengths, are usually the largest components of the
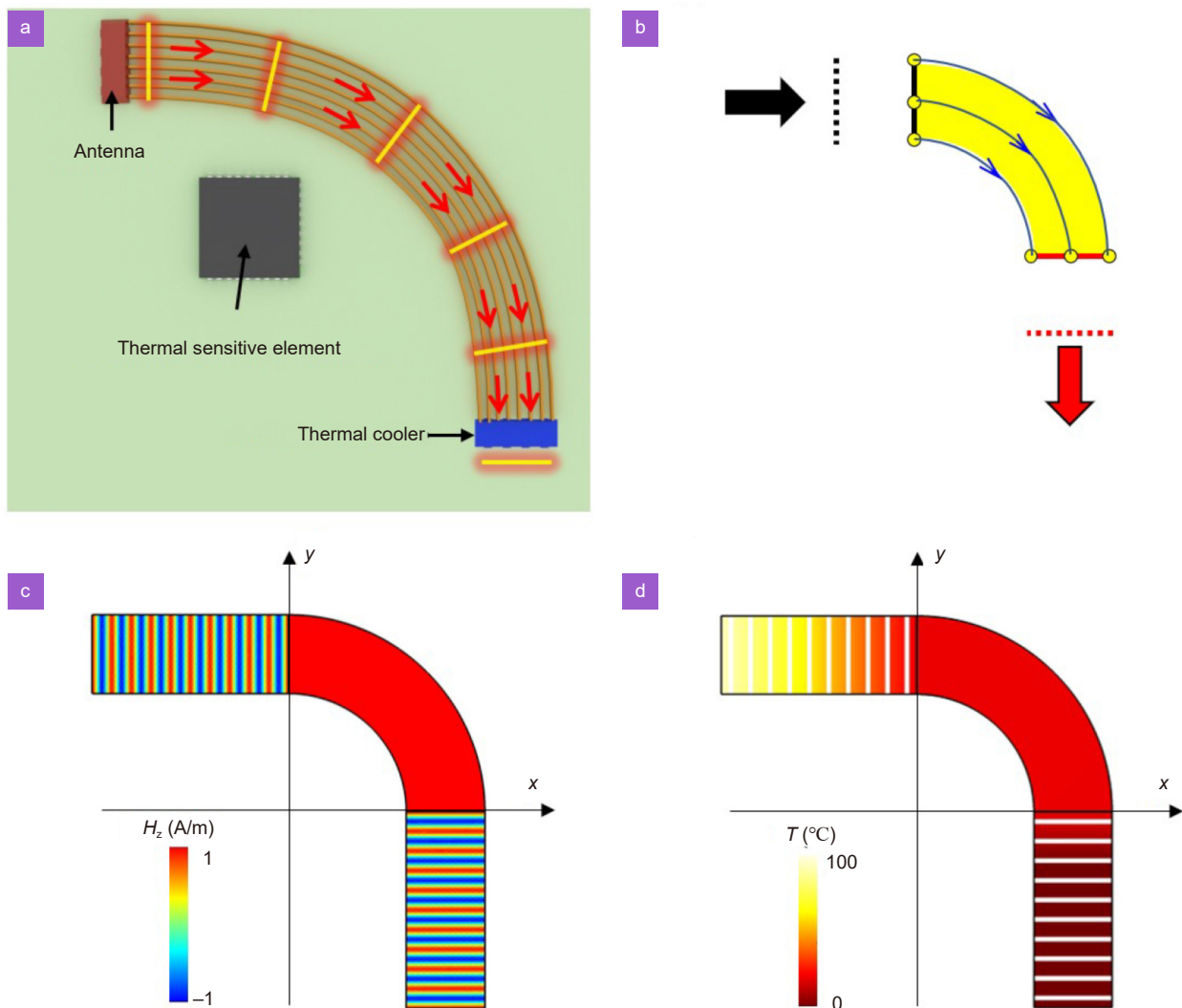
on-chip system[S5]. Most fundamental types of on-chip antennas (i.e., monopole, dipole, and loop) cannot create a directional radiation[S6]. Although the on-chip Yagi-Uda antennas can provide a directional radiation, i.e., the radiated EM waves are only from the left or right side, whose directivity is also limited[S7]. Therefore, it is still challenging to design an on-chip antenna with high directivity in a highly integrated on-chip system.

A thermal-electromagnetic cylinder-to-plane converter in Fig. S3(a), which can convert the cylindrical EM radiation produced by an on-chip loop antenna to a plane wave with high directivity, can be designed to improve the directivity of the radiated EM waves and increase the receiving efficiency of the antenna. In addition, for the waste heat generated from the on-chip loop antenna, the thermal-electromagnetic cylinder-to-plane converter can also serve as a heat spreader, which can improve the heat dissipation efficiency of the antenna. Figure S3(b) shows the design schematic diagram of the thermal-electromagnetic cylinder-to-plane converter by the thermal-electromagnetic surface transformation through standardized black-box designing steps:

Step 1: determine the input/out wavefront/isotherm, which are cylindrical surface and plane, and are shown as dashed black arc and red line in Fig. S3(b), respectively.

Step 2: determine the shape of the input and output boundaries of the TENM, which are represented by the solid black arc and red line in Fig. S3(b). The input boundary is chosen as the concentric arc of the input wavefront/isotherm, and the output boundary is chosen the same as the output wavefront/isotherm.

Step 3: design a one-to-one projection/mapping geometrically from the points on the input boundary (the solid black arc) to the points on the output boundary (the solid red line). The blue arrowed segmented polylines in Fig. S3(b) are chosen to link the input and output boundaries.

Step 4: the thermal-electromagnetic cylinder-to-plane converter can be realized by filling TENM into the yellow re-
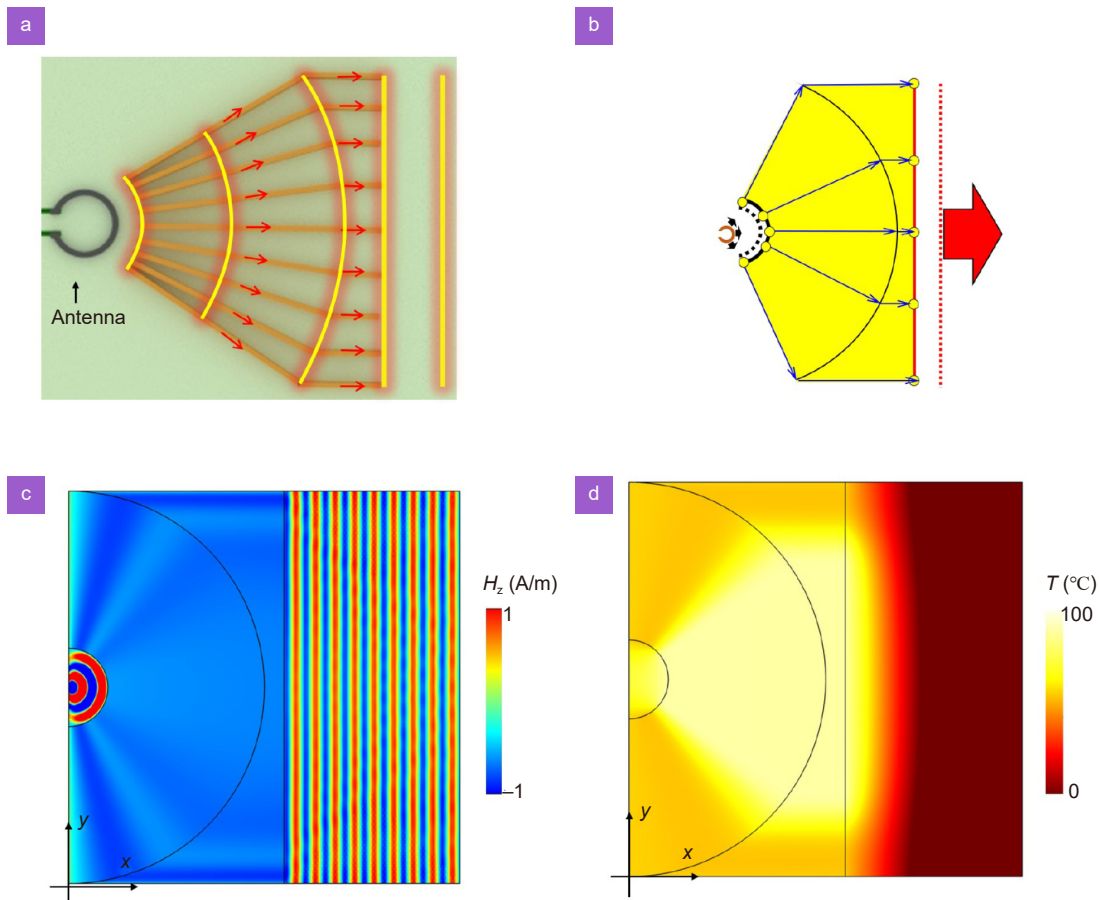

Fig. S3 | (**a**) An application of the thermal-electromagnetic cylinder-to-plane converter for on-chip system. (**b**) Design schematic diagram of the thermal-electromagnetic cylinder-to-plane converter. Simulation results for (**c**) z-component of the magnetic fields and (**d**) temperature fields for the thermal-electromagnetic cylinder-to-plane converter.

gion between the input and output boundaries in Fig. S3(b). The principal axes of the designed TENM have the same directions as the blue arrows.

The designed thermal-electromagnetic cylinder-to-plane converter can convert a cylindrical EM beam created by an on-chip loop antenna to a plane EM wave with high directivity, which is numerically verified in Fig. S3(c). At the same time, waste heat generated from the loop antenna can also directionally spread by the designed thermal-electromagnetic cylinder-to-plane converter to protect the module from high temperature, which is numerically verified in Fig. S3(d).

Thermal-electromagnetic multiplexer

For a highly integrated on-chip system, congestion among different signal channels is a common issue. For example, assuming multiple optical waveguides are used for optical communication. However, some region can only accommodate one waveguide due to the high integration level. Figure S4(a) shows this dilemma, where the cyan blocks represent the radiation/receiving module and the yellow region represents the whole unoccupied space that can be further designed to facilitate the stable communication between the radiation and receiving module. A multiplexer can be used to solve this problem. However, conventional multiplexers, e.g., wavelength/frequency/time division multiplexers, all need additional demultiplexers and other stern requirement, e.g., wavelength division multiplexer cannot work for light signals with the same wavelength.

A thermal-electromagnetic multiplexer can solve the above problem, which consists of two expanders (colored yellow) with opposite directions and several TENM channels (colored green), and is shown in Fig. S4(b). The thermal-electromagnetic multiplexer can compress all the signal channel into one and restore EM signals to the original state without additional modulation or demodulation process. These novel effects are fulfilled by the directional projection property of the TENM. Individual cooling element can be placed inside the multiplexer to achieve independent temperature control on each channel, e.g., we can place individual thermal coolers in the middle part of the TENM multiplexer to cool down some channels if their temperatures exceed the threshold of the allowed temperature value. The thermal-electromagnetic multiplexer can be designed by following the standardized black-box designing steps:

Step 1: determine the input/out wavefront/isotherm for the multiplexer, which are planes for each input/output channel.

Step 2: determine the shape of the input and output boundaries of the TENM, which are chosen the same as the input/output wavefront/isotherm.

Step 3: design a one-to-one projection/mapping geometrically from the points on the input boundary (input channel) to the points on the output boundary (output channel). The blue arrowed segmented polylines in Fig. S4(b) are chosen to link the input and output boundaries.

Step 4: the thermal-electromagnetic multiplexer can be realized by filling TENM into the yellow and green regions between the input and output boundaries in Fig. S4(b). The principal axes of the designed TENM have the same directions as the blue arrows.

Simulation results are shown in Fig. S4(c), where 5 beams with different amplitudes are compressed to a single TENM waveguide (middle part of the multiplexer) and recovered to its original distribution at the output boundary of the TENM multiplexer. The independent channel cooling effect is shown in Fig. S4(d), where we assume channels 1 and 3 need to be cooled down.

Thermal-electromagnetic cloak

Figure 3(e–h) in the main text show the cloaking effect of the thermal-electromagnetic cloak. The comparative simulations without the designed thermal-electromagnetic cloak in Fig. 3(e–h) are given in Fig. S5(a–d), which shows both EM waves and heat flows are hindered by the concealed region, i.e., the amplitude of the EM waves is smaller after the concealed region and the heat flux becomes weaker. The concealed region can be designed with other shape, e.g., a circular region in Figs. S5(e–h). Magnetic field distributions with and without cloak is shown in Fig. S5(e) and S5(g), respectively, and temperature distributions with and without cloak is shown in Fig. S5(f) and S5(h), respectively.
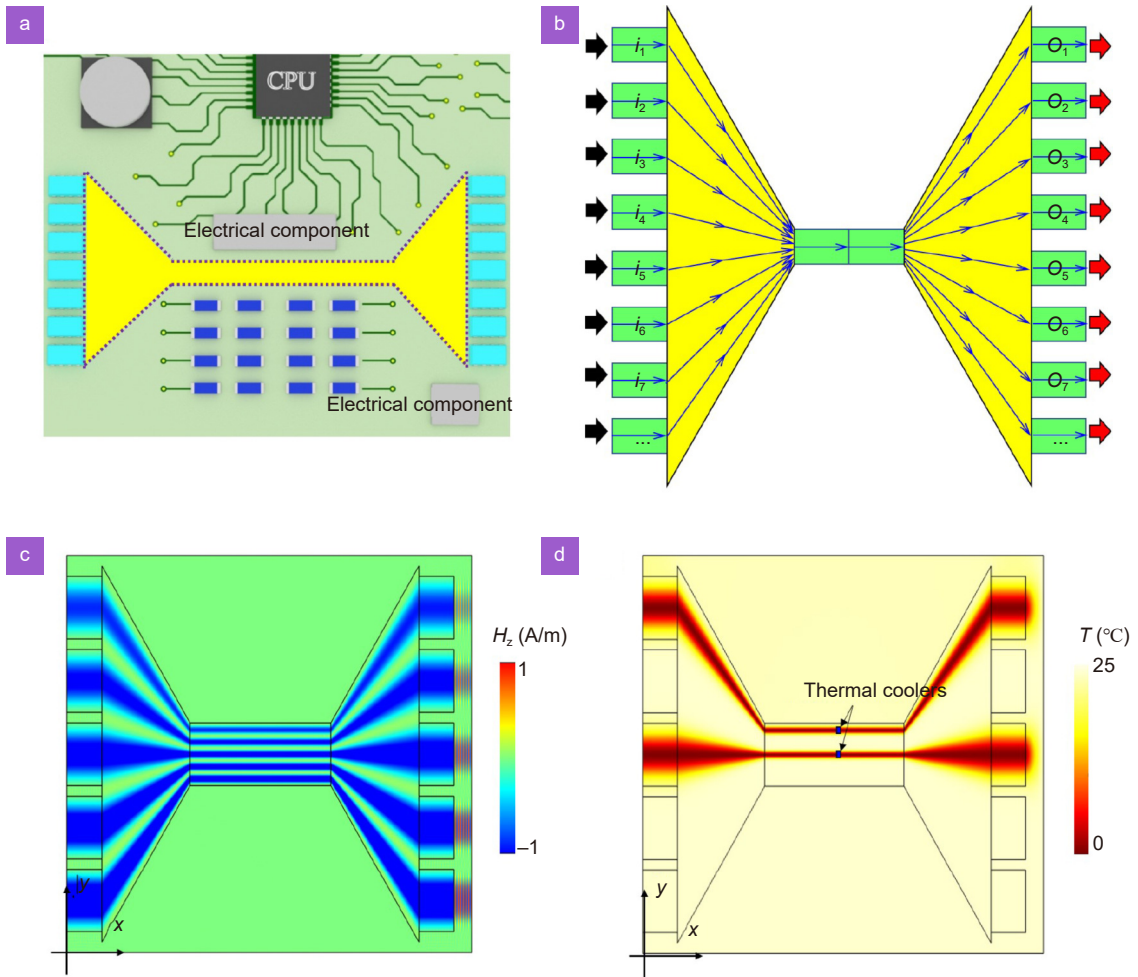
Fig. S4 | (**a**) Situation of an on-chip system where a multiplexer is needed. (**b**) Design schematic diagram of the on-chip multiplexer. Simulation results for (**c**) *z*-component of the magnetic fields and (**d**) temperature fields with the multiplexer.

Section 3: The Effective parameters, bandwidth and efficiency of the reduced TENM

Effective medium theory

The effective permittivity and permeability of two layered media with subwavelength separations, which performs as a 1D structure (see Fig. S6(a)), have been derived in previous studies, which can be summarized as[S8,S9]:

$$\begin{cases} \dfrac{1}{\varepsilon_\perp} = \dfrac{f_1}{\varepsilon_1} + \dfrac{f_2}{\varepsilon_2} \\ \varepsilon_{//} = f_1\varepsilon_1 + f_2\varepsilon_2 \\ \dfrac{1}{\mu_\perp} = \dfrac{f_1}{\mu_1} + \dfrac{f_2}{\mu_2} \\ \mu_{//} = f_1\mu_1 + f_2\mu_2 \end{cases}, \tag{S1}$$

where ε_i and μ_i (i=1,2) are permittivity and permeability of two isotropic media, respectively. $f_i=d_i/(d_1+d_2)$ is the filling factor of the i-th medium. Next, we derive the effective medium formula for thermal fields, which is also shown in Fig. S6. Thermal conductivity along one particular direction can be expressed as:

$$\kappa = S\frac{\mathrm{d}l}{\mathrm{d}T}\frac{\mathrm{d}Q}{\mathrm{d}t}, \tag{S2}$$

where *l* is the length along propagation direction of heat flux. *S* is the cross section vertical to the propagation direction of heat flux. *t* and *T* are time and temperature, respectively. *Q* is quantity of heat. When the heat flux propagates along ⊥ direction, the thermal conductivity in Eq. (S2) can be reduced to:
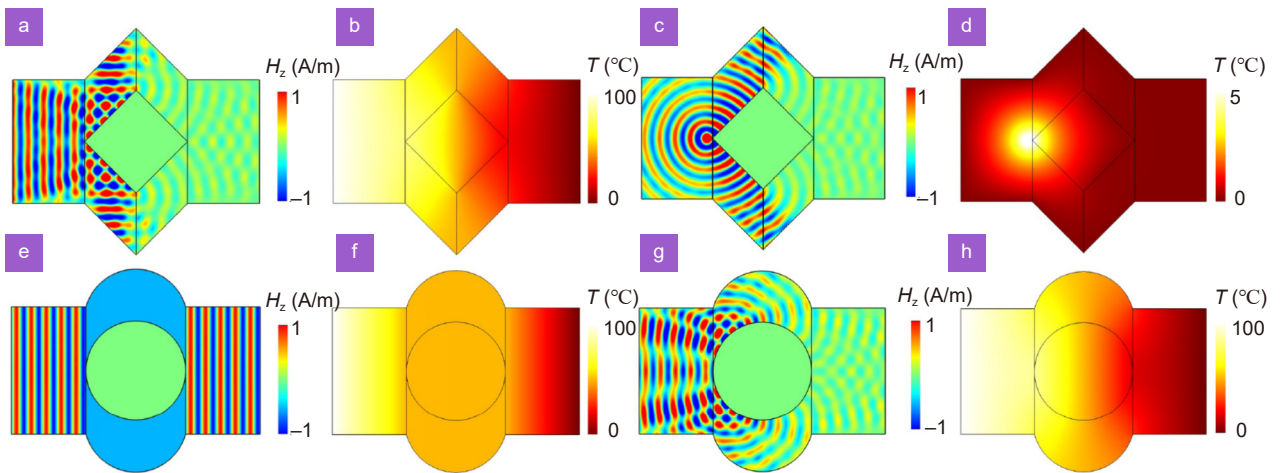
Fig. S5 | (**a–d**) Simulation results without the cloak under different type of source. (a) a plane EM wave, (**b**) a plane isotherm, (**c**) a line EM source, and (**d**) a line heat source. Simulation results for a circular concealed region under (**e**, **g**) plane EM wave or (**f**, **h**) plane isotherm (e, f) with and (g, h) without the TENM cloak.

$$
\begin{cases}
\kappa_\perp = \dfrac{1}{Hh}\dfrac{d_1+d_2}{\Delta T_1+\Delta T_2}\dfrac{\mathrm{d}Q}{\mathrm{d}t} \\[2mm]
\kappa_1 = \dfrac{1}{Hh}\dfrac{d_1}{\Delta T_1}\dfrac{\mathrm{d}Q}{\mathrm{d}t} \\[2mm]
\kappa_2 = \dfrac{1}{Hh}\dfrac{d_2}{\Delta T_2}\dfrac{\mathrm{d}Q}{\mathrm{d}t}
\end{cases}, \tag{S3}
$$

where h is the height out of the paper plane, and H is the height along $\perp$ direction. After some mathematical calculations on Eq. (S3), we can obtain:

$$
\begin{cases}
\dfrac{1}{\kappa_\perp} = \dfrac{f_1}{\kappa_1} + \dfrac{f_2}{\kappa_2} \\[2mm]
f_1 = \dfrac{d_1}{d_1+d_2} \\[2mm]
f_2 = \dfrac{d_2}{d_1+d_2}
\end{cases}. \tag{S4}
$$

Similarly, when the heat flux propagates along $/\!/$ direction, we have:

$$
\begin{cases}
\kappa_{/\!/} = \dfrac{1}{(d_1+d_2)h}\dfrac{H}{\Delta T}\dfrac{\mathrm{d}(Q_1+Q_2)}{\mathrm{d}t} \\[2mm]
\kappa_1 = \dfrac{1}{d_1 h}\dfrac{H}{\Delta T}\dfrac{\mathrm{d}Q_1}{\mathrm{d}t} \\[2mm]
\kappa_2 = \dfrac{1}{d_2 h}\dfrac{H}{\Delta T}\dfrac{\mathrm{d}Q_2}{\mathrm{d}t}
\end{cases}. \tag{S5}
$$

After some mathematical calculations on Eq. (S5), we can obtain:

$$
\kappa_{/\!/} = \kappa_1 f_1 + \kappa_2 f_2 . \tag{S6}
$$

The effective permittivity, permeability and thermal conductivity of two layered isotropic media can be summarized by Eqs. (S1), (S4) and (S6), which is Eq. (6) in the main text.

To find the best value of the EPS's filling factor for optimizing the bandwidth of electromagnetic wave's transmittance and heat transporting efficiency, we numerically study the EM transmittance in Section *The bandwidth of the reduced TENM* and the heat transporting efficiency in Section *Heat transporting efficiency of the reduced TENM* for different EPS's filling factors.

The bandwidth of the reduced TENM
For the staggered copper and EPS plates shown in Fig. S6(b), the field transmittance (defined by the magnitude of the

ratio of the transmitted EM fields and incident EM fields) in normal direction is obtained by numerical simulation. The period of the staggered copper and EPS plates is fixed to be p = 6 mm, the length of the plates is fixed to be l_0 = 282 mm (=2l in the main text), and the filling factor of the EPS is set to have some different values, i.e., f_2=w/p=0.9, 0.5, and 0.1. The transmittances are shown in Fig. S6(c), which show a broad bandwidth can be obtained by a large filling factor of EPS. As the filling factor of EPS decrease, a larger anisotropic value exists in the reduced TENM medium, which makes a larger impedance mismatch of the medium to the air, thus leading to a narrow bandwidth. Note the bandwidth cannot be promoted by reducing p (for the fixed filling factor f_2), which only makes the staggered copper and EPS plates closer to the model of effective anisotropic medium.

The following conclusions are summarized from the above discussion:

1) When the filling factor f_2 is larger than 0.5 (i.e., filling factor of metal is smaller than that of EPS), the reduced TENM is almost impedance matched to the air, and the transmittance is over 80% from 6 to 10 GHz, i.e., a broadband high transmittance for EM waves (see the green and red lines in Fig. S6(c)). Therefore, we get one conclusion in the main text "the staggered media in Fig. 4 performs as a better EM null medium for a smaller filling factor of copper".

2) When the filling factor f_2 is smaller than 0.1 (i.e., the filling factor of metal is much larger than that of EPS), large transmittance only occurs under Fabry–Pérot condition, i.e., $2l_0 = m\lambda$, where more strict frequency selection condition is needed for the staggered copper and EPS plates to be treated as TENM (see the blue and black lines in Fig. S6(c)). That the reason why we state "the staggered media performs as a poorer EM null medium for a larger filling factor of copper" in the main text.

3) In the experiment, f_2 = 0.5 is used. As the transmittance is high for a broad bandwidth, the cloak has a broadband performance. The best (at 8.97 GHz, correspond to the highest transmittance in Fig. S6(c)) and worst (at 9.24 GHz, correspond to the lowest transmittance in Fig. S6(c)) cloaking performance are shown in Fig. S6(d), which shows the worst case still has satisfactory cloaking effect. The cloaking effect at other working frequencies are also shown in Fig. S6(d), which shows the designed cloak has broadband performance from 6 GHz to 10 GHz.

Heat transporting efficiency of the reduced TENM

For thermal fields, larger filling factor of EPS means lower effective thermal conductivity, while smaller filling factor of EPS means larger effective thermal conductivity. The heat flux at the output port of the above reduced TENM (l_0 = 282 mm, p = 6 mm) with different filling factors of EPS is shown in Fig. S6(e), which shows the heat transporting efficiency drops rapidly when the filling factor of EPS is larger than 0.7. The simulated temperature distribution with filling factor of f_2 = 0.02 and f_2 = 0.98 is shown in Fig. S6(f), where large temperature contrast is observed inside the TENM with f_2 = 0.98, which indicates a low heat transporting efficiency. These numerical simulations verify that "the staggered media performs as a better thermal null medium for a larger filling factor of copper, while the staggered media performs as a poorer thermal null medium for a smaller filling factor of copper".

Summarizing the conclusions of Section *The bandwidth of the reduced TENM* on the effect of the EPS's filling factor on the bandwidth of the electromagnetic transmittance, and Section *Heat transporting efficiency of the reduced TENM* on the effect of the EPS's filling factor on heat transporting efficiency, we get the conclusion in the main text "As the staggered media performs as a better thermal null medium but a poorer EM null medium for a larger filling factor of copper, while the staggered media performs as a better EM null medium but a poorer thermal null medium for a smaller filling factor of copper".

The effect of overall scaling in size on cloaking effects

The size of the cloak can be designed at will according to the actual situation. However, the width of the staggered copper/EPS is restricted by the working frequency. If the working wavelength is much smaller than the period of the TENM structure (e.g., $\lambda < p/5$), the staggered copper/EPS structure cannot be treated as an effective medium, and therefore cannot guide wave smoothly as the TENM. Therefore, we cannot simply scale up the sample to achieve a larger cloak, the period of the staggered copper/EPS structure should also be redesigned based on the new working frequency. For thermal fields, there are no restrictions on the performance of the cloak, and the designed EM cloak can also work well for the thermal fields.

Therefore, for the sample used in the experiment, with the assumption of fixed working frequency, we can come to the following conclusions: 1) If the size of the sample is increased in equal proportion, the cloaking performance for EM waves will decrease, and the cloaking performance for thermal fields remain the same. 2) If the size of the sample is decreased in equal proportion, the cloaking performance for both the EM waves and thermal fields remain unchanged.

Section 4: The sample and 'on-chip structure' preparation.

Sample preparation

The sample preparation can be divided into four steps, which is shown in Fig. S7 and described below,

1) Copper plates with cross-section of 10 mm×3 mm, length of 141 mm, and cutting angle α = 45° at two ends are fabricated by laser cutting. The copper has thermal conductivity of 400 W/m/K and electric conductivity of 6.4×10^7 S/m, which can be regarded as good thermal conductor for heat and perfect electric conductor for microwaves.

2) Expanded polystyrene (EPS) plates with cross-section of 10 mm×3 mm, length of 141 mm and cutting angle α = 45° at two ends are fabricated by hand. The EPS has thermal conductivity of 0.04 W/m/K and relative permittivity of 1, which can be treated as static air for both temperature fields and microwaves.

3) Align one copper plate and one EPS plate carefully by the ends to form a pair. 92 pairs of copper-EPS plates are finally prepared.

4) Assemble all the copper-EPS pair around a rectangular boundary, which consists of 4 copper plates with the same size in step 1). Glue the touching copper ends along the central line of the sample by cyanoacrylate glue. EPS board with size of 141 mm×141 mm×10 mm is placed in the central region to prevent thermal convection.

'On-chip structure' Preparation

1) Prepare a large foam board with size 440 mm×616 mm×100 mm and thermal conductivity of 0.04 W/m/K.

2) Prepare two identical thin thermal pads with size 120 mm×208 mm×2 mm and thermal conductivity of 13 W/m/K.

3) Place the two thermal pads (colored blue in Fig. S7) and the sample on the surface of the foam board to mimic an on-chip operating environment.

All the required components for the sample and on-chip environment preparation are listed as below:

1) 96 copper plates with cross-section of 10 mm×3 mm, length of 141 mm, and cutting angle α = 45°;

2) 92 Expanded polystyrene (EPS) plates with cross-section of 10 mm×3 mm, length of 141 mm and cutting angle α = 45°;

3) Thermally conductive silicone grease with thermal conductivity of 6.0 W/m/K;

4) Two thermal pads with size 120 mm×208 mm×2 mm (http://www.sg-thermal.com);

5) Cyanoacrylate glue;

6) Polystyrene foam boards with size of 500 mm×500 mm×3 mm and thermal conductivity 0.035 W/m/K;

7) 16 pyramid absorbers (QYH-J200, length of 500 mm and width of 500 mm).

Section 5: The experimental setup and measurement on thermal fields

Details of experimental setup on thermal fields

The construction of experimental environment for the thermal measurement can be divided into five steps.

1) The sample is sticked on a large EPS board with size 440 mm×616 mm×100 mm. Then two thermal pads with size of 120 mm×208 mm×2 mm and thermal conductivity about 13 W/m/K are placed on the form board next to the left and right boundary of the sample. Blackbody paint (VK887) is applied on the upper surface of thermal pads and concealed region to keep a constant thermal emission coefficient.

2) Preparing the heat source. A silicone rubber heating plate with size of 400 mm×25 mm×2 mm and rated power of 18.5 W is placed (with thermally conductive silicone grease) on the left edge of the left thermal pad, which serves as a heat source with constant power. The heating plate is connected to an adjustable power supply (MCH-K-3010D-III), which can control the power of the heat source.

3) Preparing the heat sink. A 4-core semiconductor refrigerator with size of 200 mm×190 mm×145 mm is used as the heat sink, and the temperature of its top flat surface can be controlled by a matching power supply. The top surface of
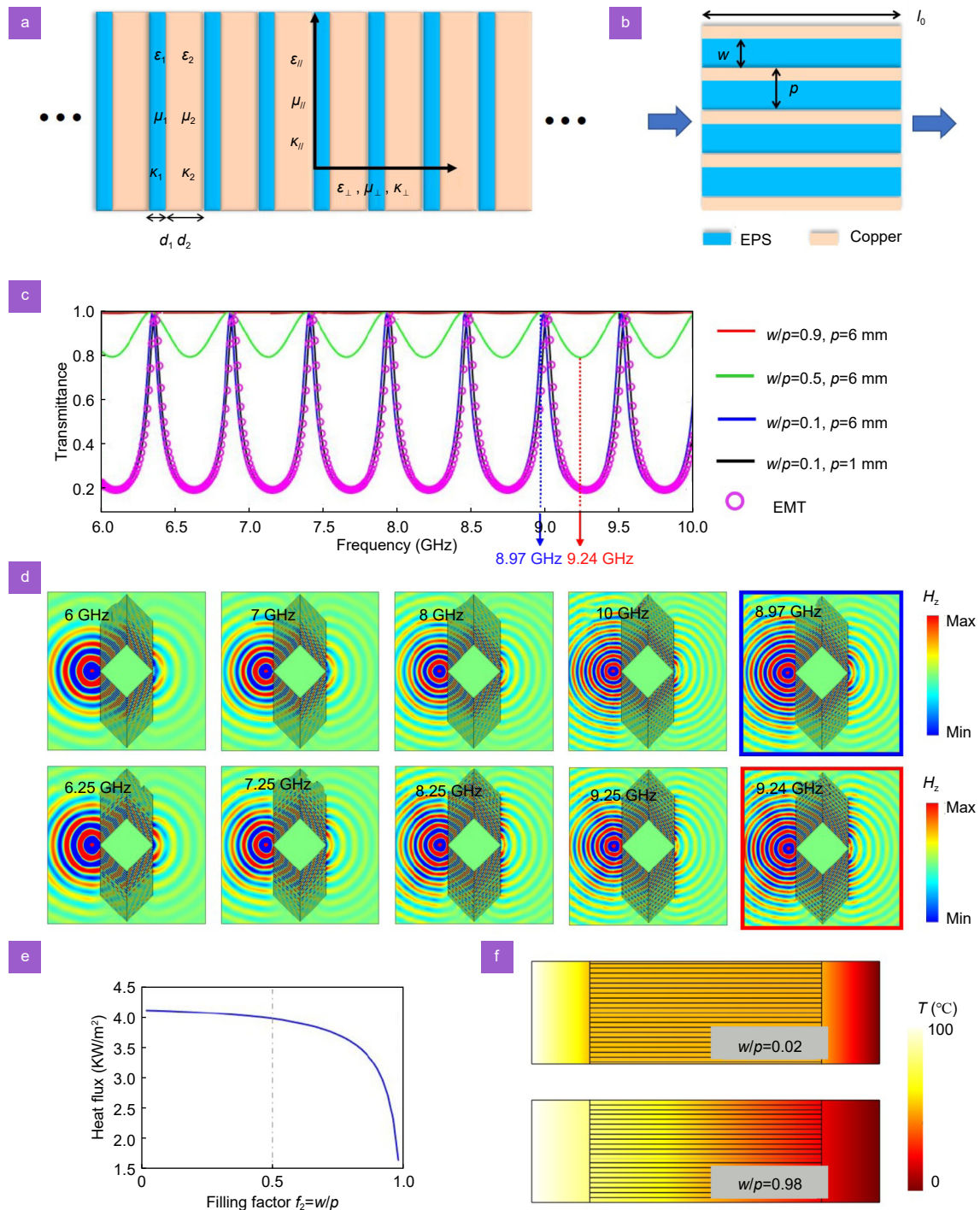
Fig. S6 | (**a**) The 1D grating structure composed by two layered isotropic media. (**b**) EM waves (blue arrow) propagate across the staggered copper and EPS plates. (**c**) Numerical simulated transmittance of the EM waves in (b) for different filling factors and periods. The purple circles represent the analytically calculated results for the effective anisotropic slab with filling factor $f_2 = w/p = 0.1$ (modeled by effective medium theory, EMT). (**d**) EM cloaking effect for different working frequencies from 6 GHz to 10 GHz. (**e**) Heat transporting efficiency with different filling factor of EPS. (**f**) Temperature distribution when the filling factor approaches 0 (top subplot) and 1 (bottom subplot).

the semiconductor refrigerator is attached to the right edge of the right thermal pad.

4) A cubic EPS shell with height of 15 mm without bottom is covered on the whole sample to prevent thermal convection and at the same time make the system reach thermal equilibrium faster.

5) An IR camera is fixed on a tripod, and its field view is adjusted to aim at the sample. The IR camera can give a visu-
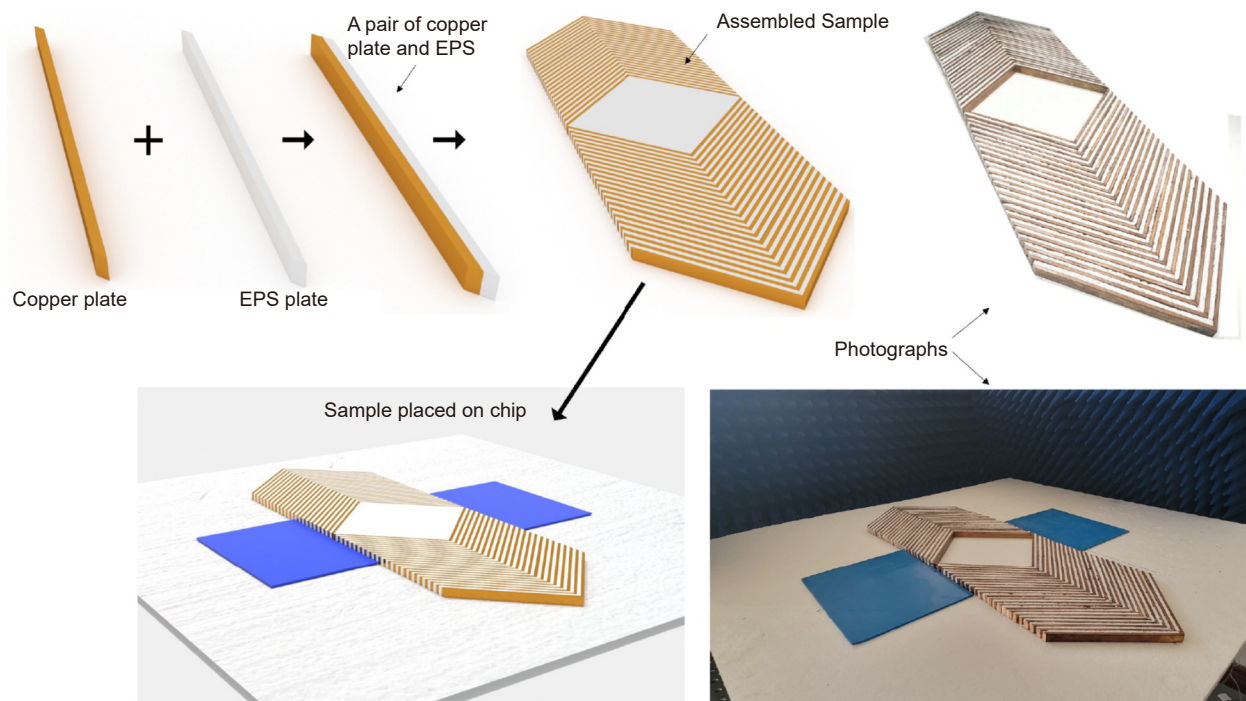
Fig. S7 | Preparation steps of the sample. The assembled sample consists of 96 copper plates (including the central 4 plates forming the boundary) and 92 EPS plates.

al real time temperature distribution of the sample. The IR camera is FOTRIC 288 (more information can be found in https://www.fotric.com).

Details of measurement on thermal fields

The temperature measurement can be divided into three steps.

　1) Firstly, power the heat source, and adjust the voltage to 7 V and the current to 0.82 A. The heat source can keep a constant temperature about 80° after 10 minutes.

　2) Power on the semiconductor refrigerator and tune its temperature to 0°. The top surface of the semiconductor refrigerator can keep a constant temperature about 0° after 20 minutes.

　3) Wait until the whole system reach the steady state, when the temperature of the sample doesn't change. Then remove the EPS shell and immediately taking pictures of the sample by the IR camera. Then power off the power supply for both the heat source and heat sink.

　For the temperature measurement of the reference without cloak, background thermal pad is used to replace the cloak shell.

　The key components and the whole experiment setup during the temperature measurement are shown in Fig. S8.

Section 6: The experimental setup and measurement on electromagnetic waves

Details of experimental setup on electromagnetic waves

The construction of experimental environment for the measurement of EM waves can be divided into four steps.

　1) Place the sample and the EPS board on an absorber base (1000 mm×1000 mm), which consists of four pyramid absorbers (QYH-J200, length of 500 mm and width of 500 mm).

　2) Fix a loop antenna on the EPS board with a distance of 30 mm from the left boundary of the sample. Central align the antenna and the sample in y and z direction. The loop antenna is made by curving a radio frequency probe (KTR 141-50, length of 100 mm and diameter of 0.94 mm) to a split ring with diameter about 4 mm. The fixed loop antenna is used as the radiation source, which is connected to one port (Port 1) of the vector network analyzer (VNA,
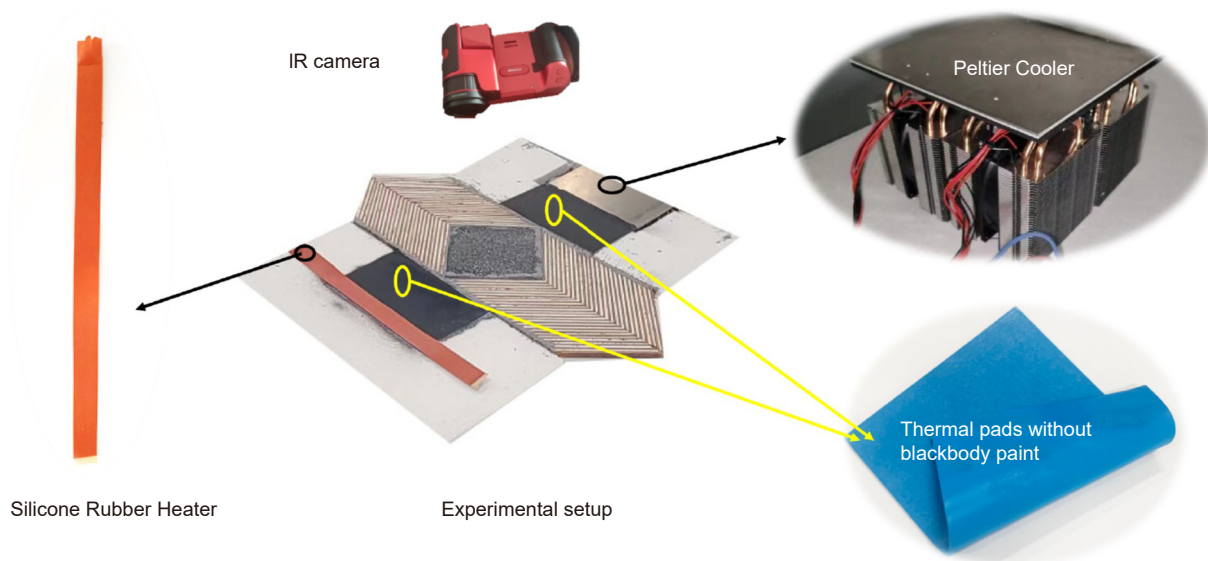
Fig. S8 | Photographs of the heat source (left subgraph), IR camera (top subgraph), experimental setup (central subgraph), thermal pad (right top subgraph) and heat sink (right bottom subgraph).

ROHDE&SCHWARZ ZVL13).

3) Make another loop antenna the same size as the source antenna, which serves as the receiving antenna and is placed 30 mm away from the right boundary of the sample. The receiving antenna is also central aligned in *z* direction and can move freely along *y* direction, which can measure magnetic fields along the detection line (indicated by the black dots Fig. 5(f) and 5(g)). The receiving antenna is connected to the other port (Port 2) of the VNA by coaxial cable.

4) Fix 8 pyramid absorbers for four sides (two for each side) of the sample and use a large absorber with four pyramid absorbers as the top absorber and covered on the sample to form a microwave anechoic chamber.

Details of measurement on electromagnetic waves
The EM fields measurement can be divided into three steps.

1) Set the range of the radiation frequency of the VNA to be 7 GHz –11 GHz, and then use the calibration kit to calibrate the VNA.

2) Divide one side of the detection line (30 mm away from the right boundary of the sample and central aligned in *z*-direction with the sample) into 23 segments with equal intervals. Mark the end points of the 23 segments, thus obtain 24 marked points. Then measure the magnetic fields with the receiving antenna at 24 marked points. During the measurement, a form board with 5 mm height is placed under the receiving antenna to make it central aligned with the sample in *z*-direction. The receiving antenna is moved from one point to another by hand after each measurement, and the position error is controlled within 1 mm.

3) Export the measured magnetic fields at the designed wavelength $\lambda_0 = 100/3$ mm from VNA for postprocessing. Take and normalize the amplitudes of measured magnetic fields at 24 marked points. Once the normalized magnetic fields at 24 marked points on one side of the detection line are obtained, the normalized magnetic fields on the other side of the detection line can be directly obtained by using the symmetry of the whole system in the *y*-direction. Then, the normalized amplitudes of magnetic fields along the whole detection line with the cloak are obtained and plotted by the red dots in Fig. 5(h).

For the measurement of the corresponding magnetic fields without cloak, the cloak is removed (leaving only the inner 4 copper plates to mimic an on-chip scatter), while keeping the other on-chip structure unchanged. Then, repeat the same three steps above to obtain the normalized amplitudes of magnetic fields along the detection line without the cloak (i.e., the blue dots in Fig. 5(h)).

The key components for the measurement of EM waves are shown in Fig. S9, and the whole experiment setup during the measurement are shown in Fig. S10.
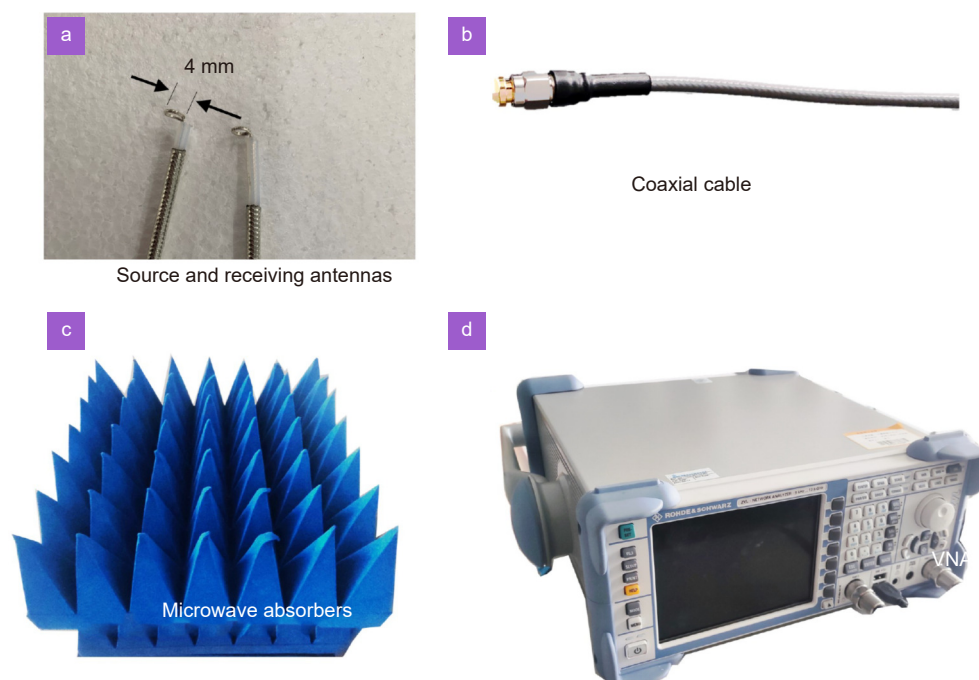
Fig. S9 | Photographs of key components during the EM measurement. (**a**) Source and receiving antennas. (**b**) Coaxial cables. (**c**) Microwave absorbers. (**d**) Vector network analyzer.
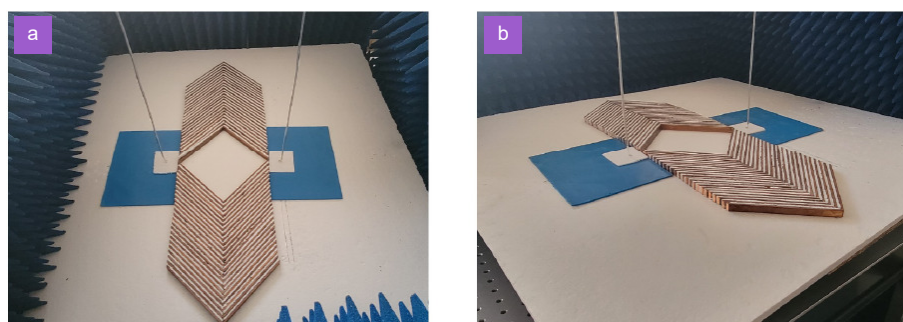

Fig. S10 | Photographs for the whole experimental setup. (**a**) Top view. (**b**) Perspective view. Microwave absorbers at the two sides are removed for a clear perspective view.

Movie S1: The whole graphic design process

Movie S2: The function of thermal-electromagnetic cloaking in the on-chip system

References

S1. Moore JP, McElroy DL, Graves RS. Thermal conductivity and electrical resistivity of high-purity copper from 78 to 400 °K. *Can J Phys* **45**, 3849–3865 (1967).

S2. Zhang H, Fang WZ, Li YM, Tao WQ. Experimental study of the thermal conductivity of polyurethane foams. *Appl Therm Eng* **115**, 528–538 (2017).

S3. Stephan K, Laesecke A. The thermal conductivity of fluid air. *J Phys Chem Ref Data* **14**, 227–234 (1985).

S4. Ranut P. On the effective thermal conductivity of aluminum metal foams: review and improvement of the available empirical and analytical models. *Appl Therm Eng* **101**, 496–524 (2016).

S5. Rotaru M, Ying LY, Kuruveettil H, Rui Y, Popov AP et al. Implementation of packaged integrated antenna with embedded front end for bluetooth applications. *IEEE Trans Adv Packag* **31**, 558–567 (2008).

S6. Cheema HM, Shamim A. The last barrier: on-chip antennas. *IEEE Microw Mag* **14**, 79–91 (2013).

S7. Hsu SS, Wei KC, Hsu CY, Ru-Chuang H. A 60-GHz millimeter-wave CPW-Fed Yagi Antenna fabricated by using 0.18-um CMOS technology. *IEEE Electron Device Lett* **29**, 625–627 (2008).

S8. Tang SW, Zhu BC, Jia M, He Q, Sun SL et al. Effective-medium theory for one-dimensional gratings. *Phys Rev B* **91**, 174201 (2015).

S9. Sun F, He SL. Extending the scanning angle of a phased array antenna by using a null-space medium. *Sci Rep* **4**, 6832 (2014).